PNAS RESEARCH ARTICLE | NEUROSCIENCE

A tool for monitoring cell type–specific focused ultrasound neuromodulation and control of chronic epilepsy

Keith R. Murphy[a], Jordan S. Farrell[b], Juan L. Gomez[c,d], Quintin G. Stedman[e], Ningrui Li[f], Steven A. Leung[f], Cameron H. Good[g], Zhihai Qiu[f], Kamyar Firouzi[e], Kim Butts Pauly[f], Butrus Pierre T. Khuri-Yakub[e], Michael Michaelides[c,d], Ivan Soltesz[b], and Luis de Lecea[a,1]

Edited by Marcus Raichle, Washington University of School of Medicine, Mallinckrodt Institute of Radiology and Department of Neurology, St. Louis, MO; received April 19, 2022; accepted September 16, 2022

Focused ultrasound (FUS) is a powerful tool for noninvasive modulation of deep brain activity with promising therapeutic potential for refractory epilepsy; however, tools for examining FUS effects on specific cell types within the deep brain do not yet exist. Consequently, how cell types within heterogeneous networks can be modulated and whether parameters can be identified to bias these networks in the context of complex behaviors remains unknown. To address this, we developed a fiber Photometry Coupled focused Ultrasound System (PhoCUS) for simultaneously monitoring FUS effects on neural activity of subcortical genetically targeted cell types in freely behaving animals. We identified a parameter set that selectively increases activity of parvalbumin interneurons while suppressing excitatory neurons in the hippocampus. A net inhibitory effect localized to the hippocampus was further confirmed through whole brain metabolic imaging. Finally, these inhibitory selective parameters achieved significant spike suppression in the kainate model of chronic temporal lobe epilepsy, opening the door for future noninvasive therapies.

neuroscience | focused ultrasound | neuromodulation | photometry | epilepsy

Temporal lobe epilepsy is highly refractory to pharmacological therapies, with limited nonsurgical options for epileptiform control. Focused ultrasound (FUS) has emerged as a next-generation tool for noninvasive neuromodulation of deep brain structures (1–9). While FUS maintains exquisite spatial specificity, its ability to modulate discrete cell types within specific brain regions is unclear. Optogenetic studies in chronically epileptic mice have demonstrated that selective activation of hippocampal parvalbumin interneurons can powerfully suppress seizures (10). However, whether FUS selectively modulates parvalbumin activity and is capable of suppressing epileptiform activity remains to be determined.

The possibility of FUS cell type specificity was highlighted in early studies of the saphenous and sciatic nerves, which found that smaller-diameter C-fibers were more sensitive to ultrasound suppression than parallel beta, gamma, and alpha fibers (11, 12). A more recent study found that excitatory, but not inhibitory, cell types of the somatosensory cortex responded to variation in ultrasound pulse repetition (13). In aggregate, the diversity of ultrasound neuromodulation findings support a nonuniversal cell type response to defined FUS parameters, probably related to both intrinsic mechanosensory channel expression, membrane properties, and network interactions of specific cell types (8, 14–19). To resolve these discrepancies across brain regions and independent studies, new tools to examine this differentiation are needed.

Fiber photometry is a widely used technique that allows researchers to record neural activity by using an optical fiber stereotactically implanted immediately above a brain region of interest. Neural activity is inferred from optical recording of genetically encoded calcium or voltage sensors that can be targeted to specific cell types within the brain region of interest. To augment this technique, we created a lightweight piezoelectric ring transducer stack that directly integrates with the fiber optic cannula to deliver FUS to discrete regions of the rodent brain. While the cannula placement controls lateral positioning, the ring shape creates a natural ultrasound focus that can be adjusted vertically with a set screw shaft collar to adjust along the dorsoventral axis (Fig. 1 *A* and *B* and *SI Appendix*, Fig. S1). To increase ultrasound transmission from the stack, a pseudo air-backed layer made of balsa wood and a magnesium alloy matching layer are stacked above and below the piezoelectric layer, respectively. A coupling gel bracket is installed on the skull and filled with a silicone grease before the transducer is lowered to its set point. By leveraging a lateral implantation site and adjustability of the shaft collar, a large variety of cortical and subcortical brain regions can be accessed with the Photometry Coupled focused Ultrasound System (PhoCUS), and the assembly is light enough for mice to freely move during stimulation and recording (Movie S1).

Significance

Ultrasound can be focused through skull onto the deep brain, altering neural activity noninvasively. Despite its broad utility, the action of focused ultrasound on specific cell types is almost entirely unknown. Understanding cell type–specific responses to FUS would allow selection of ultrasound waveforms that engage the intended targets while limiting effects on off-target fields. We developed a system combining FUS targeting and optical recording of virally labeled deep brain cell types in freely behaving animals. We used the tool to identify a protocol for the hippocampus that selectively increases inhibitory neural activity while decreasing excitatory activity with high spatial specificity. The protocol robustly suppressed epileptiforms in a chronic epilepsy model demonstrating the tool's potential for examining experimental FUS therapies.

Author contributions: K.R.M., J.S.F., J.L.G., C.H.G., Z.Q., K.B.P., B.P.T.K.-Y., M.M., I.S., and L.d.L. designed research; K.R.M., J.S.F., J.L.G., N.L., S.A.L., C.H.G., and K.F. performed research; K.R.M., Q.G.S., B.P.T.K.-Y., and L.d.L. contributed new reagents/analytic tools; K.R.M., J.S.F., J.L.G., N.L., S.A.L., and K.F. analyzed data; and K.R.M., J.S.F., J.L.G., Q.G.S., C.H.G., K.B.P., B.P.T.K.-Y., M.M., I.S., and L.d.L. wrote the paper.

Competing interest statement: K.R.M., Q.G.S., K.F., B.P.T.K.-Y., and L.d.L. are co-inventors on a patent application assigned to Stanford University containing disclosures related to the technology described in this article.

This article is a PNAS Direct Submission.

[1]To whom correspondence may be addressed. Email: llecea@stanford.edu.

This article contains supporting information online at http://www.pnas.org/lookup/suppl/doi:10.1073/pnas.2206828119/-/DCSupplemental.

Published November 7, 2022.

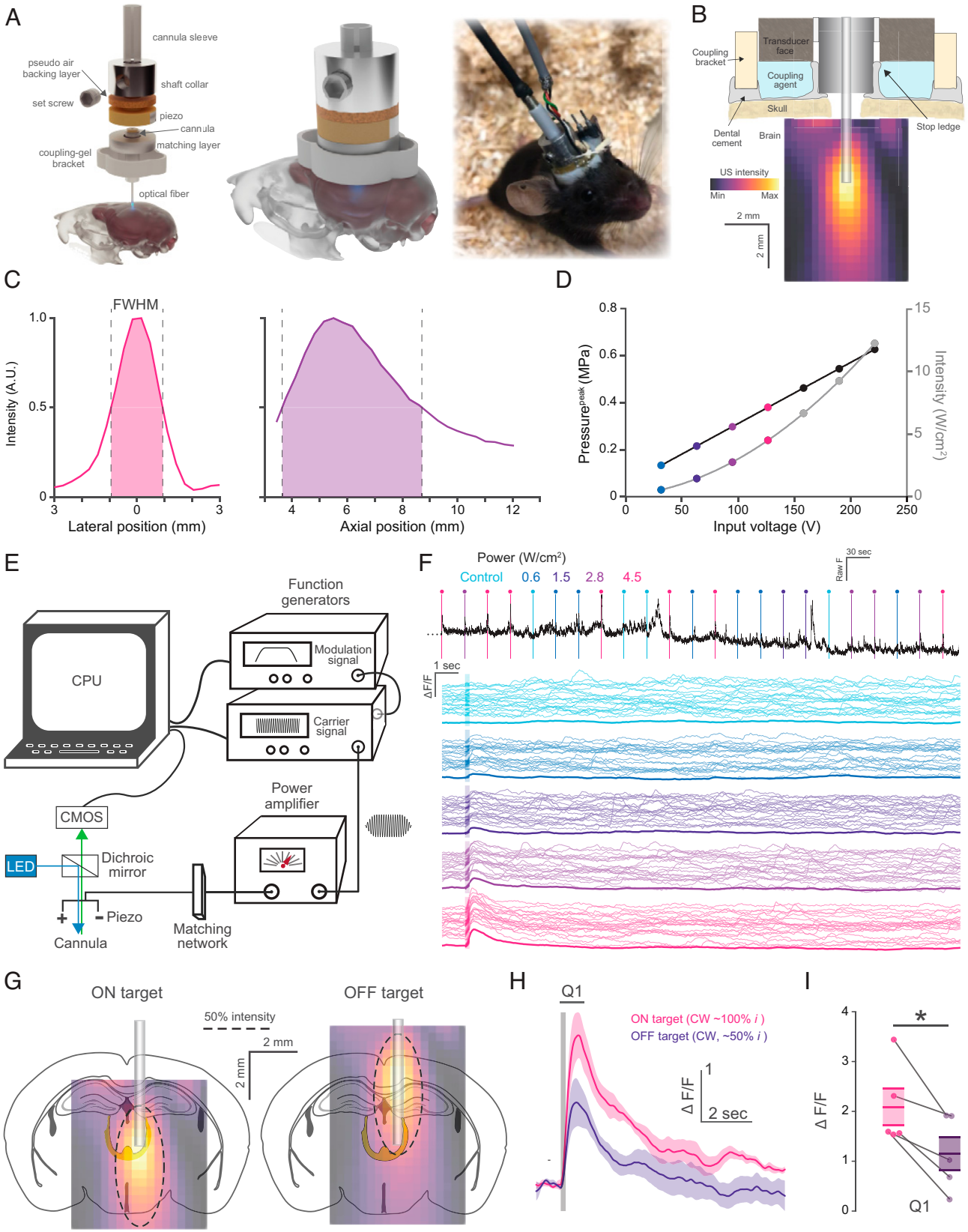

Fig. 1. A tool for integrating FUS with fiber photometry. (*A*) Exploded (*Left*), assembled (*Middle*), and real model view of the PhoCUS device. (*B*) Cross-sectional illustration of the PhoCUS device and the relative ultrasound intensity field produced in the brain. (*C*) Hydrophone characterized FWHM intensity profiles where the axial position represents distance from the transducer face. (*D*) Peak pressure and ISPPA with incremental peak input voltage. (*E*) Schematic representation of the integrated ultrasound waveform generation and photometry computational system. (*F*) Representative experiment where 200 ms continuous wave pulses of varying intensity are delivered to CAMKII+ neurons of the midbrain locomotor region in shuffled order and averaged across trials. The top black trace shows a subset of experimental signals (23/100 trials) and colored traces show all trials (thin) for each intensity and the mean (thick). (*G*) Illustration of CMT ON or OFF targeting by adjusting the transducer set height along the *z*-axis of the cannula (dash line represents FWHM boundary) (*H*) Mean cell type change in fluorescence (line) in response to continuous ultrasound pulse (gray bar, 200 ms) ($n = 5$ animals, five trials/animal, shaded area: SEM). (*I*) Quantification of Q1 period for ON and OFF target (paired *t* test; $*P = 0.014$).

Using a scanning hydrophone, we characterized the ultrasound focus of the transducer coupled to an explanted skull and found the device had a structural resonance at 623 kHz, which we used as the device operating frequency (Fig. 1*B*). The full width at half-maximum (FWHM) focal profile is ∼2 mm (lateral) by 5 mm (axial), with the peak at 5.5 mm from the radiating surface (Fig. 1*C*). After attenuation, reflection, and refraction from the skull, the focus maintained a peak negative pressure of 0.62 MPa and a spatial peak pulse average intensity (ISPPA) of 12.3 W/cm^2 with the application of a 220 peak voltage (Fig. 1*D*). To examine how the presence of the optical fiber could affect the FUS field, we simulated the radiating surface in a free field with and without the optical fiber. Simulation of the free field closely matched the shape of the measured free field, providing confidence in the simulation (*SI Appendix*, Fig. S1*A*). Simulation with a fiber present showed a slight shadowing of the ultrasound field in close proximity to the fiber tip, with the field reaching >90% intensity of the nonfiber measurement at a distance of 730 µm from the fiber tip (*SI Appendix*, Fig. S2 *A* and *B*). To compare the ultrasound field to the optical data collection area, we also measured optical collection efficiency as a function of distance from the fiber (*SI Appendix*, Fig. S2*C*). The fiber captures 45% of maximum efficiency at a distance of 0.5 mm and 20% at 1 mm. Together, these focal properties allow targeting of discrete brain regions with power in the effective range for ultrasonic neuromodulation and may be extended to other applications such as nanoparticle uncaging of compounds and microbubble-based blood–brain barrier opening (20, 21). The system software was designed to deliver randomly shuffled, fully programmable ultrasound waveforms to a given brain target while monitoring virally labeled cell types of interest; this is illustrated with a sample dataset of 200 ms continuous wave pulses delivered to a brain region at different pulse intensities (Fig. 1*E* and *F*). Complex waveform pulsing or smoothing can also be performed by signal amplitude modulation through layered function generator connections (Fig. 1*E*).

Because the transducer position can be adjusted along the *z*-axis, we examined whether calcium responses to the ultrasound focus were spatially specific. We recorded photometry signal from CAMKII+ neurons of the centromedial nucleus of the thalamus (CMT) expressing GCaMP6s and targeted the focus to the CMT directly (on-target) or to the cortical areas and skull tissue 3 mm dorsal to the target (off-target) (Fig. 1*G*). We found that the off-target stimulation induced a response that was 55% of the on-target stimulation, with similar temporal dynamics (Fig. 1 *H* and *I*). The scale of reduction suggests that the ultrasound intensity on the CMT is directly driving the response, since the off-target field is ∼50% of the on-target field. In principle, increased intensity at the skull should increase shear waves propagating to the cochlea, resulting in more audible sound (22). Since the CMT is sensitive to arousing stimuli, the lesser response of the off-target stimulation suggests that audible sound does not play a substantial role in the observed response, although it is likely there is some audibility of all discrete ultrasound waveforms examined with this system. Importantly, ultrasound waves transmitted through the skull at a 0° incidence are almost purely composed of longitudinal waves, while angles in excess of 30° are almost entirely derived from shear waves through mode conversion (23). Because the transducer face of PhoCUS is orthogonal to the midline of the skull, it likely produces less audible sound than experimental paradigms using a transducer angled toward the skull.

Fiber photometry can distinguish spatially overlapping cell types in deep brain regions by using spectrally nonoverlapping fluorophores. To examine whether overlapping cell types could have differentiated responses across ultrasound parameters, we used a viral strategy to transduce two distinct genetically encoded fluorescent calcium sensors in excitatory and inhibitory cells of the hippocampus (Fig. 2*A*). An optic fiber was implanted above the hippocampus, targeted to a site injected with an adeno-associated virus (AAV) encoding a CaMKII-promoter driven GCaMP6s and an AAV encoding CRE-dependent jRGECO1a in PV-CRE+ heterozygous mice (Fig. 2*B*). We first examined cell type responses to a 200 ms continuous wave pulse at varying pressure/intensity. Shuffled pulse protocols were delivered once every 30 s to freely behaving mice while the two-channel output was recorded. Both CaMKII+ and PV+ cells exhibited a fast rise in activity that increased with FUS intensity (Fig. 2*C*). These response kinetics were similar to those previously observed with GCaMP in cortical cultured neurons (14). Interestingly, while both cell types exhibited a fast response within 1 second after stimulation onset (peak CaMKII $\bar{X} = 445$ ms, PV $\bar{X} = 429$ ms), only PV+ cells exhibited a robust slow increase in activity 1–3 s after stimulation onset ($\bar{X} = 1.72$ s). In contrast CAMKII+ exhibited a slow decrease in activity, demonstrating a differential temporal response to FUS stimuli (Fig. 2*D*). These results suggest the possibility that PV+ cells have an additional mechanism for responding directly to FUS over a longer time course. It is also possible that the delayed response arises as a polysynaptic effect.

Given the stark differences in temporal response of hippocampal cell types during a continuous wave pulse, we questioned whether longer pulse trains delivered at high frequencies, as commonly used with FUS (8), would reveal more complex response differentiation. A pulse repetition of 900 Hz (5 s, 20% D.C., 4.5 W/cm^2 ISPPA) increased activity of hippocampal inhibitory neurons while suppressing activity of excitatory neurons, demonstrating existence of a bidirectional stimulation protocol (Fig. 3*A*). We then applied the same stimulation protocol to the ventral tegmental area (VTA) and monitored the activity of both GABAergic and dopaminergic neurons. Even in this deep brain area, we observed robust activation of inhibitory cells (Fig. 3*B*), like that of the hippocampus, and, to a lesser extent, dopaminergic neurons consistent with previous C-Fos studies (24). Interestingly, dopaminergic cells activity increased rapidly at the offset of FUS stimulation, coincident with the sharp decrease in inhibitory cell activity (Fig. 3*B*). These results raise the possibility that local interneurons are particularly sensitive to 900 Hz protocol and act to restrict the activity of excitatory cells. In agreement with this possibility, CAMKII+ neurons of the CMT, a region that does not contain local inhibitory neurons, displayed an immediate and robust increase in activity during stimulation (Fig. 3*C*). Overall, expression of the same calcium sensor under the same stimulation protocol was associated with different responses in discrete brain areas. These results support the notion that observed responses are due to intrinsic cell properties and local circuit dynamics, including interactions between excitatory and inhibitory cells, rather than artifacts related to the sensors.

To examine whether local temperature changes may play a role in the neural activity changes observed with the 900 Hz protocol (5 s, 20% D.C., 4.5 W/cm^2 ISPPA), we implanted a thermocouple attached to the tip of the optical fiber and found that temperature increased slightly at the focus after stimulation (+0.23 ± 0.15 °C absolute maximum, *SI Appendix*, Fig. S3). The focal temperature increase was an order of magnitude less than natural variations observed in mouse brain temperature, and its correlation with neural activity was not conserved in the CMT, suggesting the shift was not a dominant contributor to neural activity changes. Since the voltage and capacitance

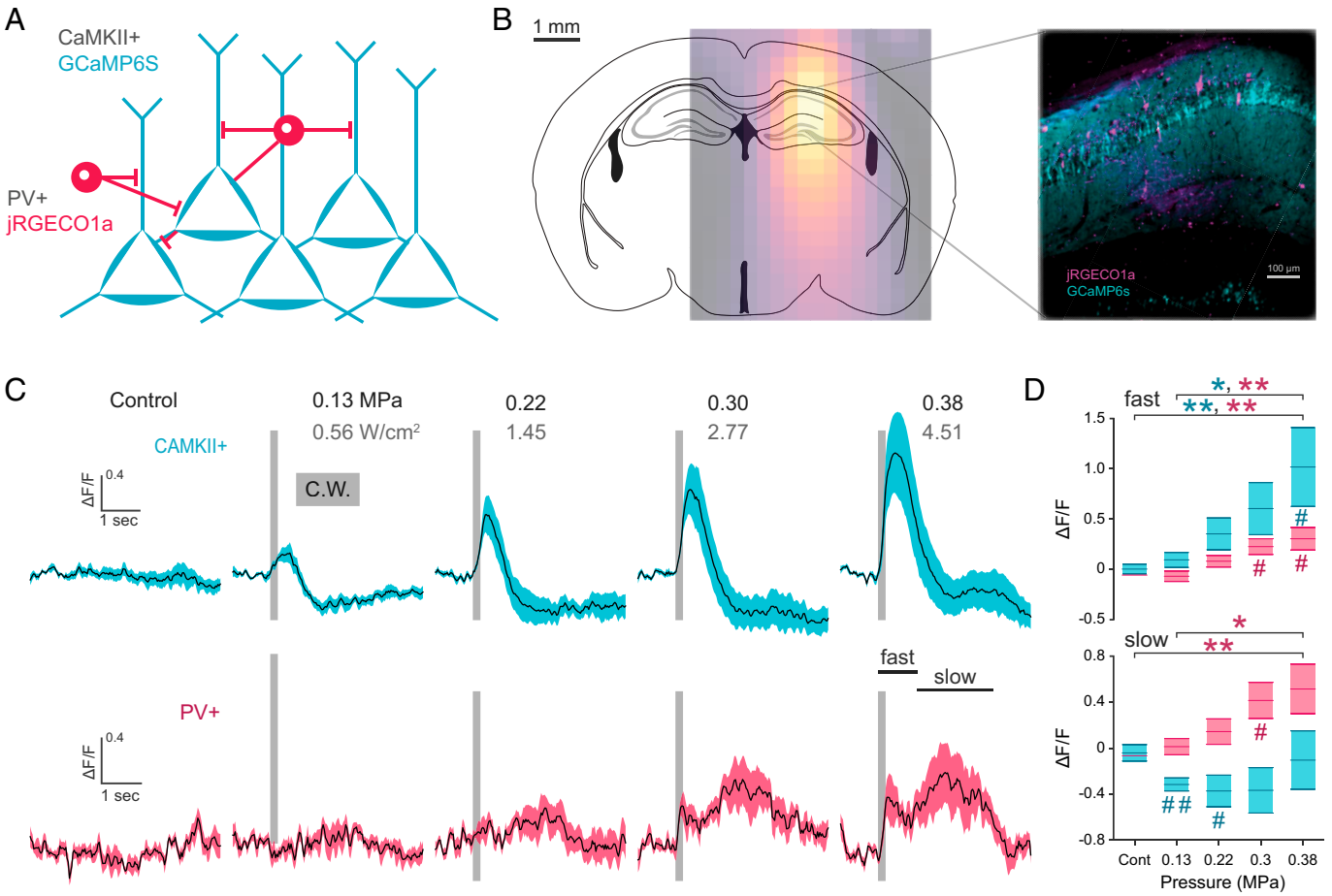

Fig. 2. Dual cell type labeling reveals temporally and directionally distinct response profiles within the FUS target network. (*A*) Genetically encoded calcium sensor labeling strategy for CaMKII+ and PV+ neural subtypes of the hippocampus. (*B*) Overlay of target hippocampal region with ultrasound intensity field and composite image of jRGECO1a and GCaMP6s within the hippocampus. (*C, D*) Mean cell type change in fluorescence (line) in response to continuous ultrasound pulse (gray bar, 200 ms) of increasing ultrasound pressure (n = 6 animals, shaded area: S.E.M.). Average fast and slow response reveals temporally variant responses between cell types of the CA1 network (one-way ANOVA, Tukey's multiple comparison test; PV-slow, $F_{4,5} = 6.85$; PV-fast, $F_{4,5} = 7.71$; CaMKII-slow, $F_{4,5} = 1.49$; CaMKII-fast, $F_{4,5} = 5.30$; *****$P < 0.05$, ******$P < 0.01$, one-sample t test; #$P < 0.05$, ##$P < 0.01$).

flux experienced by the ultrasound FUS transducer generates heat, we also measured the portion of the subcranial skull immediately below the transducer face. We observed a mild and transient heat increase (+1.2 ± 0.53 °C absolute maximum), probably caused by a combination of heat radiation from the transducer and ultrasound absorption by the skull (*SI Appendix*, Fig. S3). Intriguingly, one animal showed simultaneous temperature increase at the skull and decrease at the focal target, suggesting that the temperature changes across regions may be independent. However, interactions between changes in CSF flow (25, 26), local blood flow, and local metabolic activity (27) complicate identification of a root cause. Although both temperature changes were less than spatial or temporal variation naturally observed in the brain, users implementing more intense or longer duration protocols should consider temperature effects (*SI Appendix*, Fig. S3*C*).

To further validate the utility of PhoCUS, several concerns needed to be addressed that could not be examined by the tool itself. Fiber photometry does not collect neural activity information outside a restricted spatial domain immediately below the fiber tip, leaving the spatial specificity of the tool unknown. Furthermore, it is possible that any observed neuromodulation response may be caused by the optical fiber mechanically disturbing the tissue during ultrasound exposure (28). It is also important to replicate these findings via a translational approach capable of monitoring brain activity and facilitating potential transition to human applications. To address these concerns, we implemented whole brain metabolic imaging via positron emission tomography (PET) with the PhoCUS device during FUS stimulation of the right dorsal hippocampus in awake, freely moving mice. Importantly, these experiments lacked the optical fiber implant or skull penetration for data collection. Mice received an intraperitoneal (i.p.) injection of [^{18}F] fluorodeoxyglucose ([^{18}F] FDG) and were then placed in an open field and allowed to move freely for 30 min while [^{18}F] FDG accumulated in metabolically active brain cells (Fig. 4*A*). During this period, mice were exposed to the 900 Hz protocol (5 s, 20% D.C., 4.5 W/cm^2 ISPPA) once every 3 min for 30 min. At the end of the uptake period, mice were anesthetized and transferred to a high-resolution small animal PET scanner and scanned for 20 min. This demonstrated a highly significant ($P = 0.001$) ipsilateral decrease in brain metabolic activity within the peak pressure field, demonstrating high spatial specificity of PhoCUS neuromodulation (Fig. 4*B*). Lowering the significance threshold ($P = 0.01$), we observed suppression of broader hippocampal circuitry including CA3 tracts extending to the dorsoventral portion of the brain (Fig. 4*C*). We also performed PET imaging ($n = 3$) according to a protocol matched to the 900 Hz delivery (once every 3 min for 30 min) with a 1 Hz stimulus (5 s, 8% D.C., 4.5 W/cm^2 ISPPA) and did not observe any significant increases in FDG uptake anywhere in the brain.

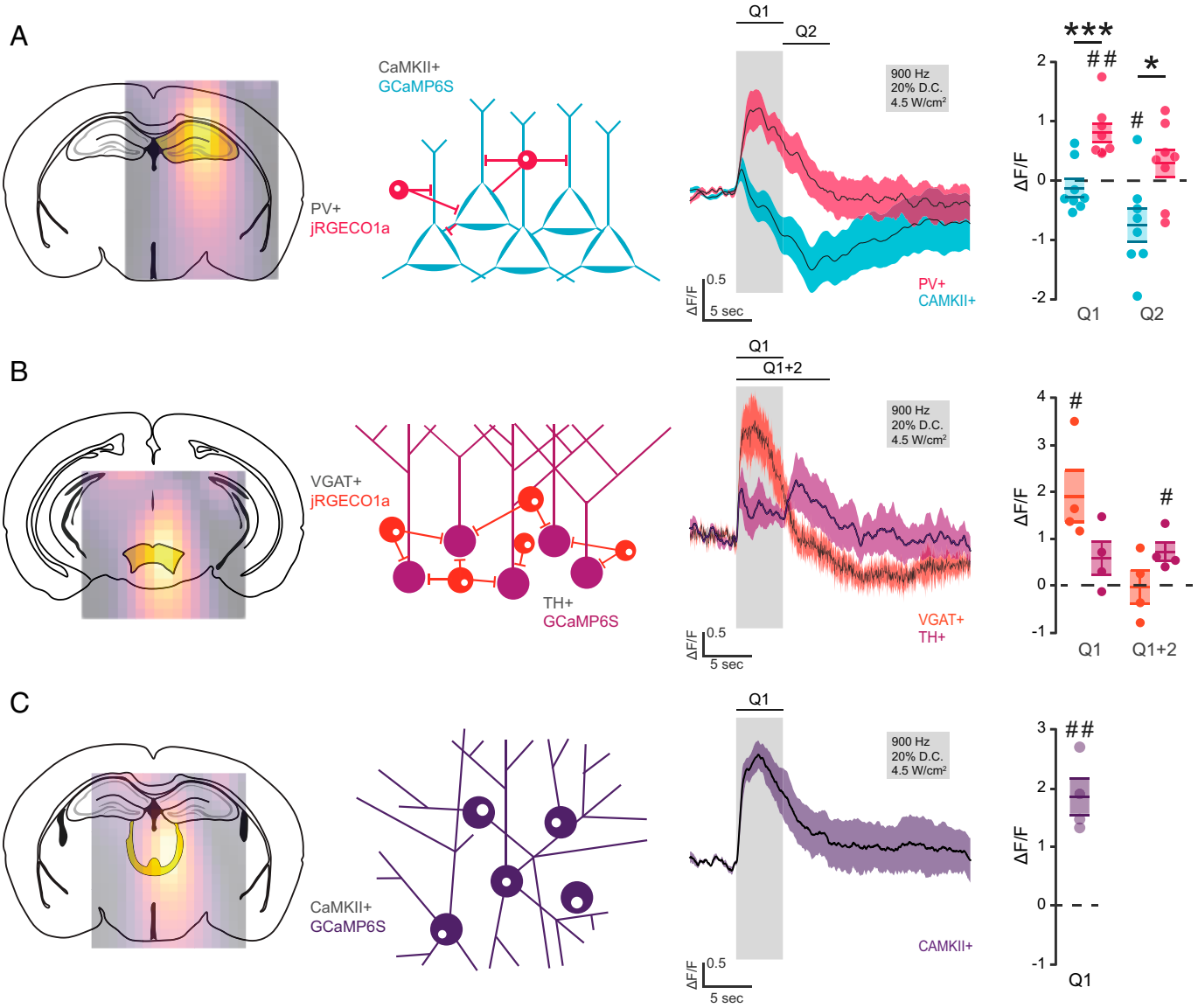

Fig. 3. Dual cell type labeling reveals directionally distinct response profiles within and across FUS target networks. (*A*) Mean cell type change in CAMKII+ and PV+ fluorescence from 5 s of 900 Hz ultrasound pulse train with quantification of fluorescence during the stimulus (Q1) and post-stimulus period (Q2) (n = 8 animals, one-sample t test, #P < 0.05, ##P < 0.01; unpaired t test, *P < 0.05, **P < 0.01). (*B*) Mean cell type change in fluorescence of simultaneously monitored VGAT+ (>JRGECO1a) and TH+ (>GCaMP6s) neurons of the VTA from 5 s of 900 Hz ultrasound pulse train with quantification of fluorescence during stimulus (Q1) and post-stimulus period (Q2) (one-sample t test, #P < 0.05). (*C*) Mean cell type change in fluorescence of simultaneously monitored VGAT+ (>JRGECO1a) and TH+ (>GCaMP6s) neurons of the VTA from 5 s of 900 Hz ultrasound pulse train with quantification of fluorescence during the stimulus (Q1) (one-sample t test, ##P < 0.01).

Given the key role of the hippocampus in temporal lobe epilepsy, we ascertained whether the 900 Hz protocol, which strongly recruited PV+ interneurons, could ameliorate epileptiform activity in a freely behaving model of chronic temporal lobe epilepsy. To this end, we unilaterally injected 200 nL of kainic acid (2.5 mM) into the right hippocampus and implanted a bipolar electrode near the site of injury to monitor epileptiform activity (Fig. 5*A*). Because the injection site undergoes extensive damage and reorganization, we targeted the contralateral hippocampus, which is as effective as ipsilateral stimulation in reducing epileptiform activity, even when the intervention is selectively targeted to PV interneurons (10, 30) (Fig. 5*A*). At 4 wk postkainate, mice experienced spontaneous high-amplitude spikes, often accompanied by high-frequency oscillations (HFOs) which are characteristic patterns of epileptiform activity (Fig. 5*B*). The 900 Hz protocol was delivered every 3 min for 5 s and rapidly suppressed epileptiform spike rate well beyond the stimulation period (Fig. 5*C* and *D*), suggesting that FUS may promote a network state less permissive for spike generation.

Collectively, this platform easily integrates with widely used fiber photometry systems and can be applied to the study of cell types, brain regions, and freely behaving animals. Insights gained from PhoCUS were instrumental in achieving type-specific control of epileptic activity. Understanding how FUS controls heterogeneous networks in a cell type specific manner is paramount in unlocking the potential for this noninvasive therapy in epilepsy and other brain disorders.

Methods

Transducer Stack Fabrication. The piezoelectric ring stack transducer was obtained from Thorlabs (part PA44LE) and has a thickness of 2 mm and an 8.3 mm outer diameter (O.D.), and the inner diameter (I.D.) was gently sanded to ~3 mm with an arc shaped Dremel tool such that the fiber photometry sleeve

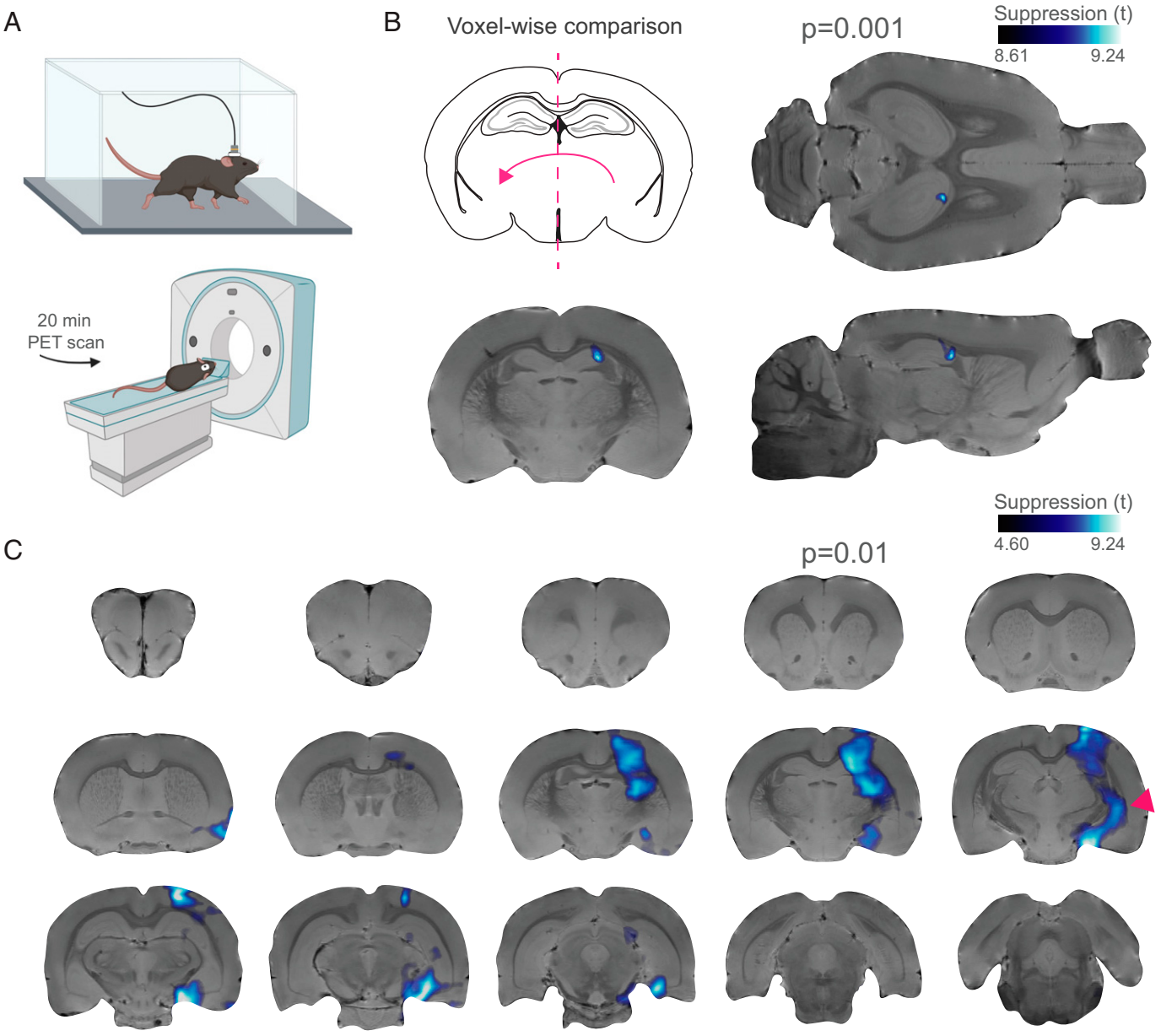

Fig. 4. 900 Hz stimulation reduces metabolic activity with high spatial precision. (*A*) Schematic of PET experiments showing freely behaving mice injected with ~400 μCi [^{18}F] FDG (i.p.) and stimulated every 3 min for 30 min during the radiotracer uptake period. Mice were then anesthetized and scanned for 20 min. (*B*) Voxel-wise analysis using statistical parametric mapping showing significant within-subject cluster differences between stimulated and unstimulated hemispheres. Voxel-wise comparisons with a probabilistic threshold-free cluster enhancement correction (29) were run with preestablished thresholds indicating a statistically significant ($n = 5$ animals, $t_4 = 8.61$, $P = 0.001$, $k > 100$) decrease in activity over the stimulated area. (*C*) Lowering statistical threshold ($t_4 = 4.60$, $P = 0.01$, $k > 100$) reveals incorporation of broader hippocampal coverage and extended networks (red arrow).

could fit through the bore. (I.D.). A one-piece set screw shaft collar (drill depth limit ring) with a single transverse set screw and 3.2 mm I.D. was obtained and machined to an 8.3 ± 0.1 mm O.D. We fabricated a matching layer by machining a 2 mm thick magnesium alloy sheet ($Z = 10.3$ MRayls) into a ring with 8.3 ± 0.1 mm O.D. and 3 ± 0.1 mm I.D. We fabricated a pseudo air-backing layer by machining a 1 mm thick balsa wood sheet into a ring with 8.3 ± 0.1 mm O.D. and 3 ± 0.1 mm I.D. Components were stacked in the following order (top to bottom): shaft collar, balsa wood, piezoelectric ring stack, magnesium alloy. To couple all the components, a thin layer of mixed two-component epoxy (Gorilla 2-part epoxy) was applied to each interfacing surface, and the stack was placed around a bare cannula sleeve. The stack was gently clamped with a rubber-plated vice tool (Irwin Quick-Grip Bar Clamp, One-Handed, Micro, 4-1/4-inch part #1964746) and allowed to cure for 24 h. Voltage leads were soldered to the piezoelectric ring stack with indium alloy solder at a 350 °F solder tip temperature. Contact time was limited as much as possible to reduce transducer heating and depoling. Ultrasound coupling brackets were custom designed and 3D printed with polyacetic acid filament with a Flashforge Creator 3 printer (see supplemental material).

Animal Genetics and Surgical Procedures. For all experiments we used adult mice (*Mus musculus*) between 8 and 24 wk old, group housed in Plexiglas chambers at constant temperature of 22 ± 1 °C and 40–60% humidity, under a normal circadian light–dark cycle (lights on at 9 AM, lights off at 9 PM). Food and water were available ad libitum. All experiments were performed in accordance with the guidelines described in the US National Institutes of Health *Guide for the Care and Use of Laboratory Animals* and approved by Stanford University Administrative Panel on Laboratory Animal Care. For photometry experiments, the following strains were used as indicated: B6;129P2-*Pvalb*$^{tm1(cre)Arbr}$/J (JAX strain #008069, PV-CRE), *Slc32a1*$^{tm2(cre)Lowl}$/J (JAX strain #016962, VGAT-CRE), C57BL/6J (JAX strain #000664), TH-FlpO::B6. For cell type–specific genetically encoded calcium indicator expression, the following AAVs were used: AAV.CamKII.GCaMP6s.WPRE.SV40 (Addgene catalog #107790), pAAV.Syn.Flex.NES-jRGECO1a.WPRE.SV40 (Addgene catalog #100853),

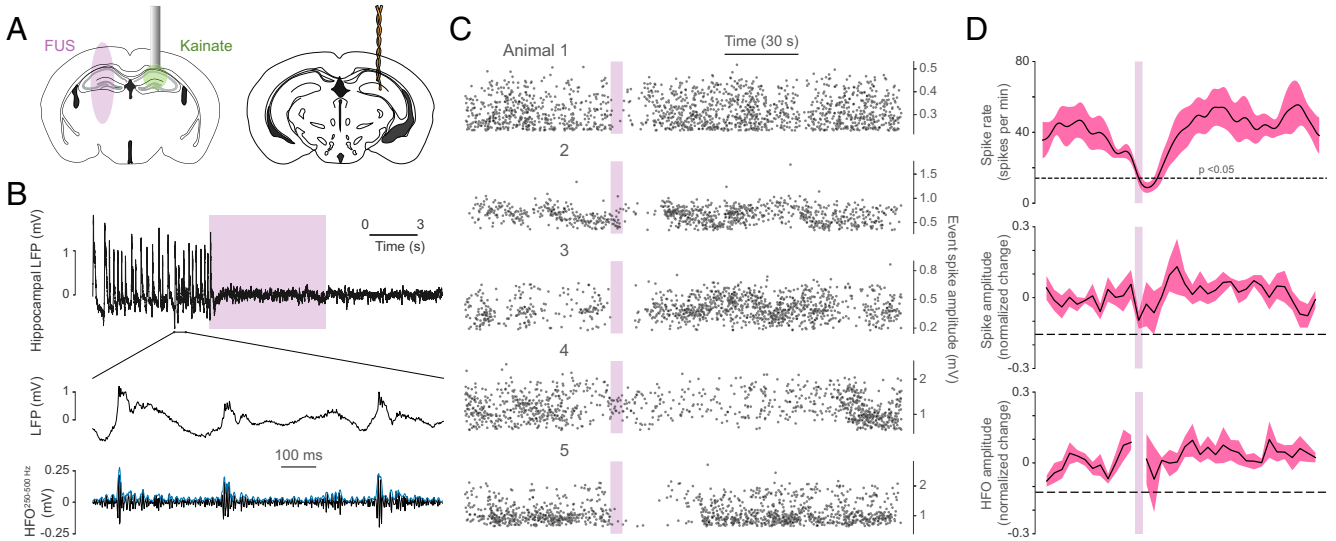

Fig. 5. 900 Hz stimulation of the contralateral hippocampus attenuates epileptiform activity. (*A*) Illustration of kainate delivery, bipolar electrode, and PhoCUS ultrasound FWHM field strategy. (*B*) Sample hippocampal local field potential (LFP) shows spontaneous epileptiform spikes accompanied by increases in HFO amplitude. Purple bar indicates ultrasound stimulation. (*C*) Ten-trial overlay of epileptiform spikes for each animal relative to ultrasound stimulation. (*D*) Mean spike rate, spike amplitude, and HFO amplitude surrounding stimulation onset (n = 5 animals, dashed line indicates the average P = 0.05 level; two-tailed).

pAAV-Ef1a-fDIO-GCaMP6s (Addgene catalog #105714). For hippocampal expression PV-CRE::B6 mice were injected with 200 nL of a 1:1 mixture of AAV.CamKII.GCaMP6s.WPRE.SV40 and pAAV.Syn.Flex.NES-jRGECO1a.WPRE.SV40. For ventral tegmental expression, VGAT-CRE::TH-FLPO mice were injected with 200 nL of a 1:1 mixture of pAAV-Ef1a-fDIO-GCaMP6s and pAAV.Syn.Flex.NES-jRGECO1a.WPRE.SV40. For CMT expression, C57BL/6J mice were injected with 100 nL of AAV.CamKII.GCaMP6s.WPRE.SV40.

For stereotactic surgery of fiber optic implants and viral injection, mice were anesthetized with a ketamine xylazine mixture (100 and 10 mg/kg i.p.) and head mounted within a stereotaxic frame (David Kopf Instruments, Tujunga, CA). To selectively express viral constructs, we infused virus through a stainless steel 28-gauge internal microinjector (Plastics One, Inc., Roanoke, VA) connected to a 10 μL Hamilton syringe. Fiber optic cannula with a 2.5 mm housing O.D. and a 400 μm fiber core (0.48 NA; Doric Lenses), were first marked along the cannula at exactly 5.5 mm from the fiber tip to indicate the distance from transducer face to the ultrasound focus. The fiber was then implanted immediately above the target brain region of interest and dental cement was formed around the cannula and skull up until the marking to create a ledge where the ultrasound transducer would be stopped along the *z*-positioning axis. A dummy transducer (see supplemental .stl files) was then secured to the coupling agent bracket and mounted to the cannula. The bracket was then carefully secured with dental cement without covering the adjacent skull surface with additional dental cement. We used the following stereotactic coordinates (in mm): hippocampus (−1.8 A/P, ±1.1 M/L, −1.9 D/V for virus; −1.8 D/V for fiber optic implants), midbrain locomotor region (−5.5 A/P, ±1.2 M/L, −2.9 D/V for virus; −3.0 D/V for fiber optic), VTA (+3.1 A/P, ±0.25 M/L, −4.3 D/V for virus; −4.1 D/V for fiber optic), and CMT (−1.27 A/P, ±0.3 M/L, −4.5 D/V for virus; −4.4 D/V for fiber optic).

Waveform Control. A PC running Windows 10 with GPIB National Instruments drivers was connected to two Agilent 33210A function generators through a GPIB-USB-HS cable to control basic pulse parameters and amplitude modulation of the carrier frequency for waveform smoothing. The function generator output was connected to a standard LC matching network (schematic of prototype can be found at https://figshare.com/articles/figure/Figure_S4_matching_network_supplemental_-01_jpg/21108994) and connected to an ENI 2100L 50 dB, 100 watt RF power amplifier. The power amplifier was connected to a matching circuit, which was connected to the transducer stack. All systems were connected with 50 ohm coaxial cables. A Python module was developed for setting ultrasound waveform characteristics during experimental paradigms (see supplemental code).

Experimental Setup. Before mounting, the animals were gently scruffed and the fiber optic patch cable was threaded through the transducer stack and coupled to the cannula. Ultrasound transducer silicone grease (Ace Hardware item #45090) was loaded into the gel coupling bracket with a small gel applicator stick. The transducer stack was then mounted to the cannula and lowered into the coupling agent; the grease should flow outside of the bracket ports, indicating the chamber is full. The set screw is turned until snug and holding the stack in place. Animals were left to habituate with ad libitum food and water access for 18–24 h before the experimental recording. All experiments were performed between ZT 3 and 8 during the light cycle.

Fiber Photometry Data Collection and Analysis. Data were collected with a Neurophotometrics FP3002 system. Importantly, any photometry system can readily integrate with the PhoCUS system. Photometry channels were sampled at 32 Hz and smoothed with a moving average window (five reads [156 ms]). Ultrasound stimulation protocols were described by prestimulation period, stimulation period, poststimulation period, duty cycle, voltage series, carrier frequency, pulse repetition frequency, and protocol repeat count. All protocol combinations were delivered regularly in a randomized order prevent chain effects. Randomization was performed by assembling arrays of all stimulus protocol iterations and shuffling with the NumPy random permutation function. We converted the photometry signal to $\Delta F/F$ by calculating the average F over the individual trial baseline period before stimulation onset via the following equation.

$$\frac{\Delta F}{F} = F\left(\frac{F - base}{base}\right) * 100,$$

where F is a fluorescence value and *base* is equal to the mean fluorescence value over a given baseline period. The baseline was considered any time before a stimulus onset for a given trial.

Because of variation in genetically encoded calcium indicator expression across animals, the dynamic range of the $\Delta F/F$ may vary substantially without representing true differences in the neural activity range. Thus, we normalized trial value differences to the mean absolute signal variation within each experiment by using the following equation. The absolute signal change was taken because positive and negative signal variation would counteract one another when we calculated mean variation.

$$F_i^{Norm} = \frac{F_i}{\sum_{|i-1|}^{N}/N},$$

where i is a single fluorescence value, N is the total number of values across an experiment, and $|i-1|$ indicates a conversion to an absolute value.

Fast and slow peak time values for the hippocampal short pulse experiments were obtained from the average time of the peak across the animal average trace for all noncontrol stimulations.

Fiber Photometry Collection Efficiency. To assess photometry collection efficiency, we attached a fiber optic probe to a stereotactic rig arm and positioned the probe orthogonal to a green fluorescent plastic. Fluorescence intensity was captured via the Neurophotometrics system CMOS camera at incremental distance between the fiber tip and the plastic.

Acoustic Wave Simulations. Simulations were performed in COMSOL Multiphysics. The geometry of the piezoelectric ring face and optical fiber were modeled from exact measurements. The fiber geometry was replaced with water for the no-fiber simulation. The speed of sound and density of water used were 1,485 m/s, and 997 kg/m^3 The speed of sound and density of the optical fiber (silica) were 5,760 m/s, and 2,650 kg/m^3 (31). Free field edges were modeled as a spherical wave radiating boundary. A pressure was assigned to the piezoelectric ring face–water boundary, and mesh size was set at $\lambda/4$. The frequency–time domain for 623 kHz was simulated, and an absolute maximum intensity was calculated from the simulated field.

Cranial Temperature Monitoring. Temperature probes were constructed from perfluoroalkoxy-insulated 70 μm diameter K-type thermocouple wire (Omega, part #5TC-TT-K-40-36). Insulation was stripped at the ends of the wires, and the brain-contacting wires were twisted and cut, yielding a short junction segment (<0.5 mm of exposed metal) to sample temperature. The other wire ends were crimped to gold-plated connectors (Eaton, part #220-P02-100). A probe was superglued parallel to the side of the glass fiber of a standard photometry optical probe, with the exposed end extending <1 mm past the fiber tip. For implantation, the photometry probe (cannula and silica fiber) was implanted in the CA1 according to the standard surgical procedure outlined above. For the subcranial probe, a 0.5 mm diameter hole was drilled in the skull at the following coordinates: 2.3 AP, −0.5 ML this region of the skull is directly underneath the radiating surface of the transducer. The probe was then slotted underneath the skull to be positioned directly above the brain and secured with dental cement. Thermocouples were implanted and a DC amplifier (Brownlee model 440) was used to amplify voltage signals by 1,000, which was digitally sampled at 5 kHz (National Instruments). Voltage versus temperature linear fits were generated in a water bath with a liquid-in-glass thermometer, ranging from 0 to 60°C, to calibrate brain temperature readings before and after the experiment. A 900 Hz, 0.2 D.C., 4.5 W/cm^2 ISPPA ultrasound protocol was delivered to the brain for 5-, 10-, or 15-s periods every 3 min, repeating at least three times per stimulation duration. Changes in brain temperature were reported from 2 to 7 s after stimulation, averaged across trials.

Acoustic Field Characterization. A cannula and bracket-mounted skull was extracted, hydrated in degassed water, and secured to the transducer stack, as performed in live animal experiments. Voltage traces resulting from ultrasound pressure waves were recorded with a fiber optic hydrophone (Precision Acoustics, Dorchester, UK) in a large, degassed water tank in a transverse plane approximately ∼2 mm from the inner skull surface to obtain the pressure at the estimated location of the focal pressure profile obtained in vivo. To prevent collision damage to the hydrophone, the photometry fiber optic probe portion on the inner surface of the skull was cleaved, which may alter the pressure field shape. Pressure and intensity were measured via square wave modulation. Spatial peak pulse average intensity (ISPPA W/cm^2) was derived from the pressures measured by the hydrophone and an estimated brain tissue acoustic impedance of 1.6 MRayls.

Intrahippocampal Kainate Model and Epileptiform Event Analysis. Mice (BLJ6, mixed-sex, 8–16 wk old) were deeply anesthetized with isoflurane and stereotactically injected with 200 nL of 2.5 mM kainic acid into the right CA1 (2.3 AP, +1.5 ML, 1.3 DV). A twisted bipolar electrode constructed from 50 μm diameter insulated tungsten wire (A-M Systems, tip separation of 0.5 mm) was implanted near the injection site (−2.5 AP, +1.65 ML, 1.3 DV) and secured with a thin layer of cyanoacrylate glue (Loctite) and dental cement (Lang) adhered to the skull. A stereotactic guide cannula was mounted to the skull according to the procedure described for the fiber photometry surgeries but did not include any fiber or skull invasion. After a minimum of 4 wk postinjection, local field potential from the hippocampus was amplified 1,000× with a differential amplifier (A-M Systems Model 1700) and digitally sampled at 5 kHz (National Instruments) with a custom Matlab (Mathworks) graphical user interface. Electrographic seizures were detected at a rate between 0.57 and 1.24 seizures per minute according to the spike frequency method definition from White et al. (2006) (32), which is consistent with previously reported seizure rates in the intrahippocampal kainate model (10). Behaviorally, these electrographic seizures were stage 0 or 1 on the Racine scale. Note that interictal spikes were also included in our analysis of spiking rates. Animals were allowed to habituate for 1 h before recording for 30 min, with one stimulation every 3 min. Epileptiform events were quantified offline in Python by band pass filtering data according to spike dynamics and locating peaks in the absolute signal (Scipy). We separated candidate events from noise by first performing principal component analysis on the raw local field potential waveforms centered within 200 ms of collected peak times followed by clustering and examination of grouped events (KMeans or DBSCAN). Spike amplitudes were reported as the absolute voltage at each peak of the filtered signal. HFO amplitude was derived from the absolute Hilbert transformation (i.e., the envelope) of the band pass filtered local field potential (200–600 Hz, third-order Butterworth). The mean HFO envelope within 100 ms centered at each peak was reported.

Ultrasound intervention timestamps were collected via the same acquisition system for recording hippocampal local field potential. We converted spike times relative to ultrasound intervention times to a rate by computing a histogram of spike times from 1 min before 2 min post-ultrasound onset (1 s bins). Data were smoothed with a one-dimensional Gaussian filter (sigma = 3). Spike amplitude and HFO amplitude were binned into 5 s segments across this 3 min interval. HFO data during the 5 s simulation bin were withheld because of the presence of high-frequency artifacts in some trials, related to the 900 Hz stimulation. To determine statistical cutoffs, spike rate, spike amplitude, and HFO amplitude were obtained from 500 iterations of randomly generated ultrasound onset times. Significance level for each measure was set to the 2.5 percentile, averaged across bins, of the shuffled distribution for each mouse.

PET Imaging. One day before scanning, mice were habituated to the open field with the transducer attached for 10 min. Mice were fasted by removing chow 1 h before lights off the day before the scan. On the day of the scan, mice were injected i.p. with [^{18}F] FDG (∼400 μCi), and stimulation was started at the same time. Uptake and stimulation were for 30 min, followed by anesthesia with isoflurane and scanning with PET (Mediso NanoScan PET/CT) for 20 min. Raw scans were reconstructed and all images were coregistered and masked to the reference mouse atlas in PMOD. Voxel-wise changes in uptake were assessed relative to global uptake between the stimulated and nonstimulated hemispheres in Statistical Parametric Mapping 12. A paired *t* test was used with a *P* value indicated in the text. A cluster threshold was set at $k = 100$ to ensure that only voxel cluster sizes equal to or greater than 100 would be analyzed, reducing noise.

Component Sourcing. Bore shaft collar, Lucas Part # BSC-012
Piezo ring chip, Thor Labs Part # PA44LE
GPIB-USB-HS WITH NI-488.2 FOR WI, Digikey Part # 2770-778927-01-ND
Agilent function generator, Keysight Part # 33210A
ENI 2100L RF 100 W 50 dB Amplifier, ENI Model # 2100
Ace Waterproof Plumbers Grease, Ace Hardware Item # 45090

Data, Materials, and Software Availability. The data reported in this work have been deposited in the figshare repository and can be downloaded from the following URL: https://figshare.com/articles/dataset/Murphy_et_al_2022_data_files/21258573 (33). All study data are included in the article and/or supporting information.

ACKNOWLEDGMENTS. Supported in part by grants from NIH (MH116470 and DA055056 to L.d.L.). K.R.M. was supported by the Ruth L. Kirschstein Postdoctoral Individual National Research Service Award (1F32HL149458-01A1) and the Multi-Institutional Training in Genetic/Genomic Approaches to Sleep Disorders Award (5T32HL110952-08).

Author affiliations: [a]Department of Psychiatry and Behavioral Sciences, Stanford University, Stanford, CA 94305; [b]Department of Neurosurgery, Stanford University,

Stanford, CA 94305; [c]Biobehavioral Imaging and Molecular Neuropsychopharmacology Unit, National Institute on Drug Abuse, Baltimore, MD 21224; [d]Department of Radiology, Johns Hopkins University School of Medicine, Baltimore, MD 21205; [e]Department of Electrical Engineering, Stanford University, Stanford, CA 94305; [f]Department of Radiology, Stanford University, Stanford, CA 94305; and [g]Querrey Simpson Institute for Bioelectronics, Northwestern University, Evanston, IL 60601

1. S. S. Yoo, H. Kim, B. K. Min, E. Franck, S. Park, Transcranial focused ultrasound to the thalamus alters anesthesia time in rats. *Neuroreport* **22**, 783–787 (2011).
2. K. Yoon *et al.*, Effects of sonication parameters on transcranial focused ultrasound brain stimulation in an ovine model. *PLoS One* **14**, e0224311 (2019).
3. R. L. King, J. R. Brown, W. T. Newsome, K. B. Pauly, Effective parameters for ultrasound-induced in vivo neurostimulation. *Ultrasound Med. Biol.* **39**, 312–331 (2013).
4. J. Kubanek *et al.*, Remote, brain region-specific control of choice behavior with ultrasonic waves. *Sci. Adv.* **6**, eaaz4193 (2020).
5. Y. Tufail *et al.*, Transcranial pulsed ultrasound stimulates intact brain circuits. *Neuron* **66**, 681–694 (2010).
6. W. Legon *et al.*, Transcranial focused ultrasound modulates the activity of primary somatosensory cortex in humans. *Nat. Neurosci.* **17**, 322–329 (2014).
7. L. Verhagen *et al.*, Offline impact of transcranial focused ultrasound on cortical activation in primates. *eLife* **8**, 1–28 (2019).
8. G. Darmani *et al.*, Non-invasive transcranial ultrasound stimulation for neuromodulation. *Clin. Neurophysiol.* **135**, 51–73 (2021).
9. T. Deffieux *et al.*, Low-intensity focused ultrasound modulates monkey visuomotor behavior. *Curr. Biol.* **23**, 2430–2433 (2013).
10. E. Krook-Magnuson, C. Armstrong, M. Oijala, I. Soltesz, On-demand optogenetic control of spontaneous seizures in temporal lobe epilepsy. *Nat. Commun.* **4**, 1376 (2013).
11. R. R. Young, E. Henneman, Functional effects of focused ultrasound on mammalian nerves. *Scienc.* **134**, 1521–1522 (1961).
12. R. R. Young, E. Henneman, Reversible block of nerve conduction by ultrasound. *Arch. Neurol.* **4**, 83–89 (1961).
13. K. Yu, X. Niu, E. Krook-Magnuson, B. He, Intrinsic functional neuron-type selectivity of transcranial focused ultrasound neuromodulation. *Nat. Commun.* **12**, 2519 (2021).
14. S. Yoo, D. R. Mittelstein, R. C. Hurt, J. Lacroix, M. G. Shapiro, Focused ultrasound excites cortical neurons via mechanosensitive calcium accumulation and ion channel amplification. *Nat. Commun.* **13**, 493 (2022).
15. B. Sorum, R. A. Rietmeijer, K. Gopakumar, H. Adesnik, S. G. Brohawn, Ultrasound activates mechanosensitive TRAAK K^+ channels through the lipid membrane. *Proc. Natl. Acad. Sci. U.S.A.* **118**, e2006980118 (2021).
16. S. J. Oh *et al.*, Ultrasonic neuromodulation via astrocytic TRPA1. *Curr. Biol.* **29**, 3386–3401 (2019).
17. M. L. Prieto, O. Ömer, B. T. Khuri-Yakub, M. C. Maduke, Dynamic response of model lipid membranes to ultrasonic radiation force. *PLoS One* **8**, e77115 (2013).
18. M. L. Prieto, K. Firouzi, B. T. Khuri-Yakub, M. Maduke, Activation of piezo1 but not $Na_V1.2$ channels by ultrasound at 43 MHz. *Ultrasound Med. Biol.* **44**, 1217–1232 (2018).
19. J. Kubanek *et al.*, Ultrasound modulates ion channel currents. *Sci. Rep.* **6**, 24170 (2016).
20. R. Chopra, N. Vykhodtseva, K. Hynynen, Influence of exposure time and pressure amplitude on blood-brain-barrier opening using transcranial ultrasound exposures. *ACS Chem. Neurosci.* **1**, 391–398 (2010).
21. M. S. Ozdas *et al.*, Non-invasive molecularly-specific millimeter-resolution manipulation of brain circuits by ultrasound-mediated aggregation and uncaging of drug carriers. *Nat. Commun.* **11**, 4929 (2020).
22. H. Salahshoor, M. G. Shapiro, M. Ortiz, Transcranial focused ultrasound generates skull-conducted shear waves: Computational model and implications for neuromodulation. *Appl. Phys. Lett.* **117**, 033702 (2020).
23. P. J. White, G. T. Clement, K. Hynynen, Longitudinal and shear mode ultrasound propagation in human skull bone. *Ultrasound Med. Biol.* **32**, 1085–1096 (2006).
24. T. Bian *et al.*, Noninvasive ultrasound stimulation of ventral tegmental area induces reanimation from general anaesthesia in mice. *Research* (2021). 10.34133/2021/2674692.
25. M. Aryal *et al.*, Noninvasive ultrasonic induction of cerebrospinal fluid flow enhances intrathecal drug delivery. *J. Control. Release* **349**, 434–442 (2022).
26. S.-S. Yoo *et al.*, Enhancement of cerebrospinal fluid tracer movement by the application of pulsed transcranial focused ultrasound. *Sci. Rep.* **12**, 12940 (2022).
27. C. M. Collins, M. B. Smith, R. Turner, Model of local temperature changes in brain upon functional activation. *J Appl Physiol (1985)* **97**, 2051–2055 (2004).
28. M. N. Collins, K. A. Mesce, Focused ultrasound neuromodulation and the confounds of intracellular electrophysiological investigation. *eNeuro* **7**, ENEURO.0213-20.2020 (2020).
29. T. Spisák *et al.*, Probabilistic TFCE: A generalized combination of cluster size and voxel intensity to increase statistical power. *Neuroimage* **185**, 12–26 (2019).
30. F. Berglind, M. Andersson, M. Kokaia, Dynamic interaction of local and transhemispheric networks is necessary for progressive intensification of hippocampal seizures. *Sci. Rep.* **8**, 5669 (2018).
31. R. Hui, *Introduction to fiber-optic communications* (2019). 10.1016/C2015-0-04508-7.
32. A. M. White *et al.*, Efficient unsupervised algorithms for the detection of seizures in continuous EEG recordings from rats after brain injury. *J. Neurosci. Methods* **152**, 255–266 (2006).
33. Murphy *et al.*, Data for "A tool for monitoring cell type–specific focused ultrasound neuromodulation and control of chronic epilepsy." Figshare. https://figshare.com/articles/dataset/Murphy_et_al_2022_data_files/21258573. Deposited 3 October 2022.